Check for updates

Self-assembled nanostructured membranes with tunable pore size and shape from plant-derived materials†

Ruiqi Dong, ‡ Na Kyung Kim,‡ Zhuan Yi and Chinedum O. Osuji *

Nanostructured materials derived from sustainable sources are of interest as viable alternatives to traditional petroleum-derived sources in membrane applications due to environmental concerns. Here, we present the development of pore size-tunable nanostructured polymer membranes based on a plant-derived material. The membranes were fabricated using a tri-functional amine as the templating core species and a cross-linkable ligand synthesized from rose oil-derived citronellol. The self-assembly of a supramolecular complex between the template core and the ligand forms a hexagonally packed columnar (Col_h) mesophase, the dimensions of which can be precisely controlled by changing the stoichiometric ratio between these constituents. Within the hexagonal mesophase stoichiometric range, the pore size of the nanostructured membranes can be tuned from 1.0 to 1.3 nm, with a step size of approximately 0.1 nm. The membranes exhibited a clear distinction in molecular size selectivity, as demonstrated by dye adsorption experiments. The membrane fabricated with a ligand-to-core ratio of 3 to 1 demonstrated shape-based selectivity, exhibiting a higher permeability for propeller-shaped penetrants and highlighting its potential for shape-selective transport. We anticipate that this straightforward approach, using plant-derived materials, can contribute to important sustainability aspects while enhancing the performance of current state-of-the-art nanostructured membranes by enabling precise control over pore size.

1. Introduction

Nanostructured materials often exhibit enhanced physicochemical properties compared to bulk systems, thus improving their performance in various applications such as catalysts, optoelectronic devices, energy storage, sensors, and antibacterial films.[1–3] In particular, due to their high surface area to volume ratio, nanostructured materials have been of the greatest interest in separation fields for filtration and adsorption.[4] Molecular species can be transported through nanostructured materials, which provides the basis for the development of nanofiltration membranes. Nanostructured membranes can also be used as adsorbents when they have distinct surface properties such as charge or polarity. Recently, there has been an increase in the utilization of sustainably sourced materials as a replacement for traditional petroleum-derived plastics in adsorbent applications. For example, activated carbon made from rice husks and hydrogels made from nanocellulose have

been utilized as adsorbents.[5–7] However, because of the irregularity of their structure, it is still challenging to selectively adsorb a specific solute among molecules of similar molecular sizes or shapes on the nm scale.

To improve the performance of adsorbents, recent interest has centered more on the creation of nanostructured membranes by self-assembly.[8,9] Self-assembly is a spontaneous process that results in the formation of ordered structures. It can be driven by microphase separation, excluded volume interactions, and other non-covalent interactions such as van der Waals, electrostatic, hydrogen bonding, and π–π stacking interactions.[10–12] Block copolymer and liquid crystal (LC) systems represent canonical examples of self-assembling molecular materials and readily form a variety of mesophases such as lamellar, columnar, and bi-continuous cubic[13–17] with interesting anisotropic transport properties.[18] 'Molecular templating' involves the use of non-covalent interactions to create supramolecular constructs that undergo self-assembly and yield precisely defined pores upon removal of the templating species. This approach has been used successfully to create membranes with uniform pores ranging from sub-nm to 10 nm.[11,19–22] For multiple uses of a single nanostructured template membrane, the pore size and functionality have been further tuned by several chemical modifications, such as

Department of Chemical and Biomolecular Engineering, University of Pennsylvania, Philadelphia, PA 19104, USA. E-mail: cosuji@seas.upenn.edu

breaking chemical bonds under basic conditions and *cis–trans* chemistry.[23,24] However, the tunable pore size spacing achieved by the post-chemical reaction hardly reaches the sub-nm level. Thus, effective separation and recovery of various impurities and resources within minor molecular size differences remain a nontrivial challenge.[20,25,26] For self-assembled systems, changes in the stoichiometry of molecular building blocks result in proportional changes in the characteristic dimension of the system. For example, in block copolymers at a constant molar mass, a change in composition (ratio of one block to another) will change the relative size of features produced by self-assembly, such as the diameter of cylinders or the thickness of lamellae.[27–29] The potential therefore exists to utilize such changes to manipulate the size of transport regulating domains with high fidelity.

Supramolecules (A–B#) constructed based on molecular templates between two complementary molecules (A and B) using fixed recognition sites are typically prepared at precise stoichiometric ratios (where # is the molar ratio of A to B). For example, Feng *et al.* formed vertically aligned nanopores in a polymer membrane using the molecular templating approach and the mesophase was composed of 3 molar ratios of conjugated linoleic acid and 1 molar ratio of 1,3,5-tris(1*H*-benzo[*d*]-imidazol-2-yl)benzene (TBIB) (CLA-TBIB3.0).[19] Off-stoichio-metric ratio mesophases have not been widely explored. Previous work has demonstrated that the self-assembly of hexagonal columnar mesophases is tolerant of some deviation from ideal functional group stoichiometry (*i.e.* overall molar ratios that deviate from the 1 : 1 functional group ratio associated with the supramolecular interaction).[30] Such off-stoichiometric ratio assembly provides a handle *via* which one may tune the pore size and potentially the pore shape as well.

Here, we demonstrate sub-nm tunability of the pore size in nanostructured membranes based on variations in the stoichiometry in a self-assembled hexagonal columnar (Col_h) mesophase. The Col_h mesophase was formed by self-assembly of discotic-shaped supramolecules composed of a template core molecule, tris(3-aminopropyl)amine (TRIS), and a polymerizable ligand compound (CL). TRIS is a liquid molecule smaller than previously reported rigid aromatic template molecules,[11,21,22] and CL was synthesized from rose-oil-derived citronellol (Fig. 1(a) and Fig. S1, S2†). We explore the effect of the stoichiometric ratio between the template molecule and the complementary ligand compound on the properties of the Col_h mesophase of the supramolecules, CL-TRIS#s. The dimensions of the Col_h mesophase are variable as the stoichiometry changes, which facilitates fine-tuning of the pore size of nanostructured membranes (Fig. 1(b) and (c)). Membranes
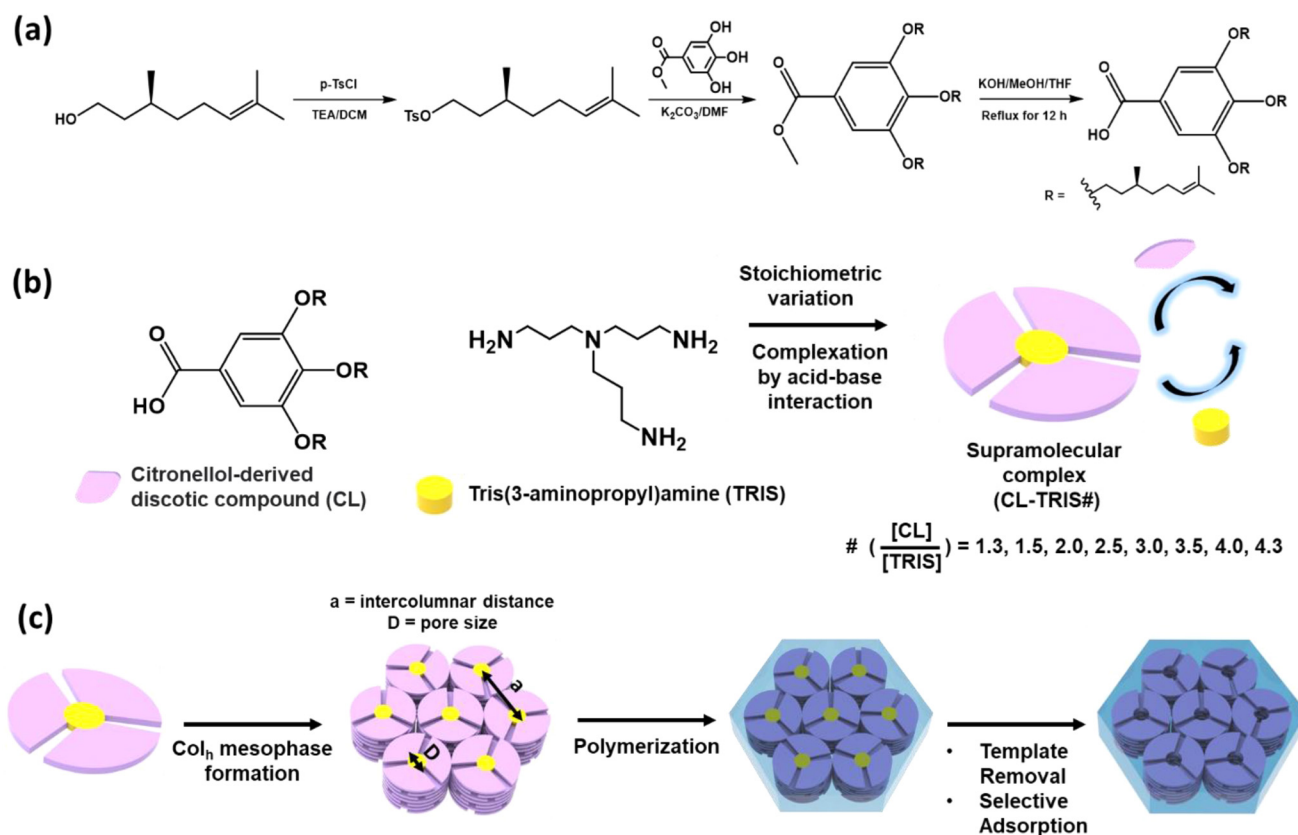

Fig. 1 (a) Synthesis procedure of a polymerizable citronellol-derived discotic LC compound (CL). (b) Chemical structure of citronellol-derived ligand compound (CL) and a template core compound, tris(3-aminopropyl)amine (TRIS), for the formation of a series of supramolecular complexes (CL-TRIS#). (c) Schematic illustration for the fabrication process of a nano-porous membrane based on the template approach.

fabricated *via* the template approach show tunable pore sizes from 1.0 to 1.3 nm with sub-nm resolution. The selectivity performances in this context were determined based on the results of dye selectivity adsorption. CL-TRIS3.0 and CL-TRIS2.0 membranes were selected for dye adsorption experiments and exhibited a clear distinction in size selectivity for molecular solutes. In addition, CL-TRIS3.0 membranes demonstrated the potential of shape selectivity to propeller-shaped molecules. We anticipate that stoichiometric control of the templated Col_h mesophase can further improve the performance of current state-of-the-art nanostructured membranes while contributing to the sustainability aspect.

2. Experimental section

2.1 Materials

All solvents purchased from Fisher Scientific were used without any further treatments. Beta-citronellol, gallic acid, *p*-toluenesulfonic acid, and TRIS were purchased from TCI, America, Inc. Triethylamine was purchased from Sigma-Aldrich. 1,6-Hexanediol dimethacrylate (HDDMA) purchased from Sigma-Aldrich was used after removal of the inhibitor by distillation. 2,2-Dimethoxy-2-phenylacetophenone (DMPA) was purchased from Sigma Aldrich.

2.2 Synthesis

1-Bromo-3,7-dimethyloct-6-en (1). 15 g of beta-citronellol (96.0 mmol) was dissolved in a mixture solvent of 200 ml of dichloromethane (DCM) and 40 ml of triethylamine in a 500 mL one-neck round bottom flask equipped with a stir bar. After the solution was cooled down to 0 °C, *p*-toluenesulfonic acid (54.9 g, 288.0 mmol) was added slowly over 10 min with stirring. As the reaction continued overnight at room temperature, insoluble salts were formed. The salts were removed by filtering and the solvent was evaporated from the filtrate using a rotary evaporator. The residue was dissolved in deionized water (DI water) and extracted with hexane. The organic phase collected was dried over anhydrous $MgSO_4$, followed by removal of the solvent. The crude material was passed through a silica gel column using hexane : ethyl acetate (99 : 1(v/v)) as the eluent. Finally, light-yellow oil could be obtained after fully drying under vacuum.

Methyl 3,4,5-tris(3,7-dimethyl-6-octenyl-1-oxy)benzoate (2). Compound **1** (10.8 g, 34.8 mmol) and K_2CO_3 (9 g, 65.2 mmol) were added to a stirred solution of gallic acid (2 g, 10.9 mmol) in 40 ml of dimethylformamide (DMF) in a 250 ml round flask. The reaction mixture was continuously stirred at 60 °C overnight. After the reaction was completed, the resulting suspension was poured into DI water and extracted with chloroform. The organic phase was dried over anhydrous $MgSO_4$, and the solvent was removed using a rotary evaporator. The residue was then purified using a silica gel column (hexane : ethyl acetate (99 : 1 (v/v))) to obtain clear oil.

3,4,5-Tris(3,7-dimethyl-6-octenyl-1-oxy)benzoic acid (CL). Compound **2** (3 g, 5.4 mmol) was dissolved in a 20 ml mixture of methanol and water (3 : 1(v/v), 40 ml) containing 10 molar equivalents of NaOH, followed by heating to 60 °C overnight. After cooling down to ambient temperature, the resulting solution was neutralized with 3.0 M HCl and extracted with chloroform. The organic phase was dried over anhydrous $MgSO_4$ and concentrated under vacuum to obtain the final product as clear oil.

2.3 Formation of CL-TRIS#s

CL and TRIS were dissolved in a mixture of chloroform and methanol (90 : 10 (v/v)) with different feed ratios of CL to TRIS (1.3, 1.5, 2.0, 2.5, 3.0, 3.5, 4.0, 4.3). The solution was shaken for 3 h under ambient conditions (22 °C) and then drop-cast on the substrates. The final products CL-TRIS#s were collected after fully drying under vacuum overnight.

2.4 Polymerization of the Col_h mesophase

A 3 mg mixture comprising CL-TRIS#s and 12 wt% of HDDMA and 1 wt% of DMPA was dissolved in a mixture of chloroform and methanol (90 : 10 (v/v)) with a concentration of 10 wt%. The mixture solution was vortexed to mix homogeneously under ambient conditions (22 °C), and subsequently drop-cast on a clean glass substrate within a 1.5 cm × 1.5 cm mold. After fully drying, a 1.5 cm × 1.5 cm × 13 μm film was polymerized under 365 nm UV light (100 W Sunspot SM spot curing system) in an N_2 environment for 3 h.

2.5 Fabrication of nanostructured membranes

3 mg polymer films were immersed in 10 ml of 0.05 wt% NaOH aqueous solution for 73 h under ambient conditions (22 °C) to remove the template molecules (TRIS). The samples were then rinsed with DI water several times to wash the residual template molecules and NaOH. The dynamic release of TRIS was monitored by time-dependent UV-Vis spectroscopy. The thickness of the nanostructured membrane remained around 13 μm.

2.6 Dye adsorption

Dye molecules including one anionic dye, rose bengal (RB), and ten cationic dyes, Basacryl red GL (BRG), basic orange (BO), toluidine blue O (TBO), auramine orange (AO), crystal violet (CV), tetrazolium blue (TB), rhodamine 6G(RH6G), alcian blue 8G (AB8G), Victoria pure blue BO (VPB), and brilliant green (BG), were employed as penetrants with a concentration of 50 μM dissolved in DI water. This low concentration was intentionally chosen to prevent the formation of clusters among the dye molecules that might occur at higher concentrations. In order to demonstrate the pore selectivity of the nanoporous membranes, adsorption tests were conducted using dye mixture solutions, in which two dyes were added with equal volume fraction and concentration. Membranes were rinsed in water for another 2 d to wash down the residual NaOH before the dye adsorption tests. In each adsorption test, a 3 mg membrane was immersed in a 14 ml volume of dye mixture solutions and shaken for 3 d until reaching equilibrium. The shaking aids in the uniform dispersion of the dye

mixture within the container, thereby preventing dye aggregation and the formation of concentration gradients. Containers were wrapped in aluminum foil to prevent photobleaching or photo-degradation of dyes under room light. The membrane was then taken out of the dye solution and the adsorption (%) was measured before and after immersion using a Cary 300 UV-Vis spectrophotometer. All photos of the dye solutions were taken at 48 h to observe the color change.

2.7 Characterization methods

Differential scanning calorimetry (DSC). The thermal transition behaviors of the polymers were analyzed through differential scanning calorimetry (DSC) with a TA instrument DSC 2500 under an N_2 atmosphere. Samples weighing 3–7 mg were encapsulated in sealed aluminum pans. The samples were quenched to 0 °C, then heated from 0 °C to 100 °C and cooled back to 0 °C at a rate of 5 °C min^{-1}. Fig. S6† summarizes the heating processes of all samples.

Polarizing optical microscopy (POM). POM images were obtained using a Zeiss Axiovert 200M inverted microscope with crossed-polarizers. All samples were annealed at a heating and cooling rate of 5 °C min^{-1} prior to taking POM images.

Small-angle X-ray scattering (SAXS). SAXS measurements were performed using a XENOCS Xeuss 2.0 system X-ray scattering instrument at the University of Pennsylvania. The instrument was equipped with a GeniX3D Cu beam source with a wavelength of $\lambda = 1.54$ Å. Silver behenate was used as the standard for calibrating the distance between the detector and the sample. All 2-D scattering patterns were integrated into 1-D plots of scattering intensity (I) versus q using Foxtrot software. Unpolymerized mesophase samples, polymer films, and nanostructured membranes were sandwiched between polycarbonate films and scattered for 10 min to collect the signals.

UV-Vis spectroscopy. UV-Vis spectra were recorded using a Cary 300 spectrometer.

Fourier transform infrared (FT-IR) spectroscopy. FT-IR spectra of the samples were recorded using an FTIR (JASCO 6300) in attenuated total reflection (ATR) mode.

Nuclear magnetic resonance spectroscopy (NMR). ^{1}H NMR spectra were recorded using a NEO400 with automation using CDCl$_3$ or MeOD-4 as the solvent.

3. Results and discussion

3.1 LC properties of CL-TRIS#s

A series of supramolecular complexes denoted as CL-TRIS#s, where # represents the molar feed ratio of CL to TRIS, were synthesized through a self-assembly process between CL and TRIS via acid–base interactions.[11,19,30] Various stoichiometric ratios, namely # = 1.3, 1.5, 2.0, 2.5, 3.0, 3.5, 4.0, and 4.3, were investigated in this study. The occurrence of acid–base interactions was confirmed by Fourier transform infrared spectroscopy (FT-IR), where the disappearance of the carboxylic acid (–COOH) peak of CL at 1688 cm^{-1} and the primary amine (–NH$_2$) peak of TRIS at 3320 cm^{-1} was observed in the FT-IR

spectrum of CL-TRIS#s (Fig. S3†). Non-ionized or ionized amine and carboxylic acid groups that may participate in making the complexes are often barely detectable by FT-IR measurements.[30] The experimental stoichiometric ratio # (#$_{exp}$) in the CL-TRIS#s complexes was further substantiated by the nuclear magnetic resonance (NMR) spectrum (Fig. S4†). In the NMR spectrum, the peaks labeled as 'a' and 'b' correspond to the protons on the benzene rings of CL and the protons on the methyl groups of TRIS adjacent to the primary amines (–NH$_2$), respectively. The experimental molar ratio of CL to TRIS, #$_{exp}$, was calculated as 3[a]/[b]. A detailed explanation is included in the caption of Fig. S4.†

CL-TRIS1.5 to CL-TRIS4.0 exhibit the Col$_h$ mesophase, while CL-TRIS1.3 and CL-TRIS4.3 remain isotropic liquids, which can be confirmed by observations from the polarized optical microscopy (POM) images and small-angle X-ray scattering (SAXS) 1D plots (Fig. S5†). Under POM, CL-TRIS1.5 to CL-TRIS4.0 show a typical fan-shaped optical texture associated with the Col$_h$ mesophase, whereas no birefringence was observed for CL-TRIS1.3 and CL-TRIS4.3.[13–15,19] The SAXS experiments indicated the presence of Col$_h$ mesophases for CL-TRIS1.5 to CL-TRIS4.0 based on the characteristic ratios of $1 : \sqrt{3} : \sqrt{4}$ for the Bragg peak locations, corresponding to the q_{100}, q_{110}, and q_{200} reflections.[14,15,19] In contrast, CL-TRIS1.3 and CL-TRIS4.3 exhibit only a single diffraction peak, indicating a lack of ordered assemblies within these systems. The Col$_h$ to isotropic transition temperature ($T_{colh-iso}$) of CL-TRIS#s was determined using POM (Fig. 2a). CL-TRIS3.0 exhibited the highest transition temperature at 99 °C, suggesting that it has the highest thermal stability, attributable to the strongest acid–base interaction at the 'optimum' stoichiometric ratio. As CL-TRIS# deviates away from the 'optimum' stoichiometric balance, $T_{colh-iso}$ gradually decreases. Differential scanning calorimetry (DSC) heating scans (Fig. S6†) agree with the POM results. However, $T_{colh-iso}$ of CL-TRIS1.5 and CL-TRIS4.0 is less detectable, likely due to the comparatively weak acid–base interaction in these systems, which may also account for the smaller diffraction peaks of d_{110} and d_{200} compared to those observed for other complexes in Fig. S5.†

3.2 Dimension of the Col$_h$ mesophase and pore size

The stoichiometric effect on the dimensions and pore sizes of CL-TRIS#s was systematically analyzed (Table 1). The intercolumnar distance, 'a', was calculated from $2d_{110}$, which mainly describes the dimension of the Col$_h$ mesophase. Meanwhile, the theoretical pore size of the Col$_h$ mesophase, 'D', is closely related to the volume fraction of TRIS in the complex (ϕ_{TRIS}) and was calculated using eqn (1). The calculation of ϕ_{TRIS} is detailed in the ESI.†

$$D = d_{100}\left(\frac{8\phi_{TRIS}}{\sqrt{3}\pi}\right)^{1/2} \tag{1}$$

The pore size is directly proportional to ϕ_{TRIS} within the system (Fig. 2b). As the hexagonal mesophase stoichiometric ratio changes from 4.0 to 1.5, ϕ_{TRIS} increases from 0.10 to 0.23,
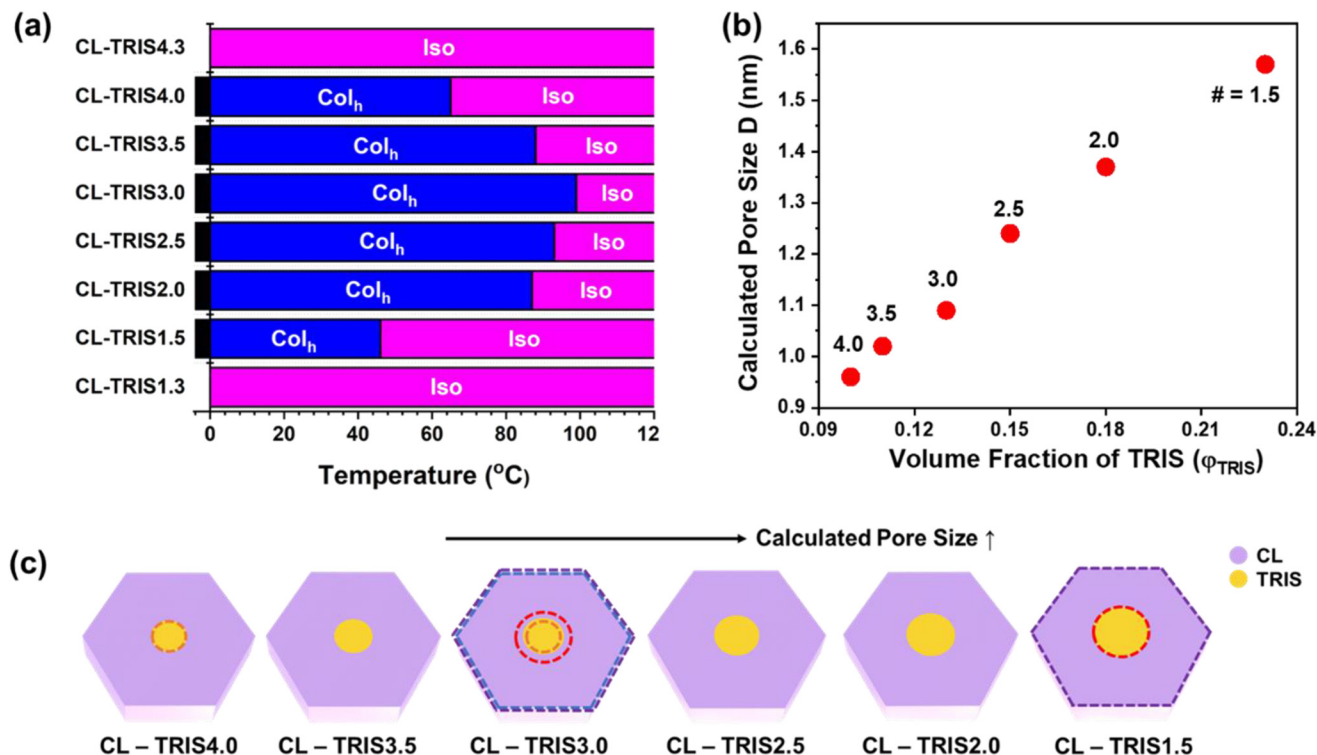
Fig. 2 (a) Phase-transition behaviors of CL-TRIS#s, which were determined by POM. Col$_h$ and iso indicate the hexagonally packed columnar meso-phase and the isotropic phase, respectively. (b) Calculated pore size, D, as a function of the volume fraction of TRIS in CL-TRIS#s, ϕ_{TRIS}. (c) Schematic diagrams of CL-TRIS#s with relative dimensions of the mesophase and pore size. The smaller orange-dotted circle in CL-TRIS3.0 rep-resents the pore size of CL-TRIS4.0 and the larger red-dotted circle represents the pore size of CL-TRIS1.5. The smaller blue-dotted hexagon rep-resents the mesophase dimension of CL-TRIS3.0, while the larger purple-dotted hexagon represents the mesophase dimension of CL-TRIS1.5.

Table 1 Structural parameters of CL-TRIS#s

CL-TRIS# (# = [CL]/[TRIS])	M_w (g mol^{-1})	d_{100} (nm)	d_{110} (nm)	a (nm)	D (nm)
CL-TRIS4.3	2522	2.56	—	—	—
CL-TRIS4.0	2360	2.52	1.47	2.93	0.96
CL-TRIS3.5	2088	2.51	1.45	2.91	1.02
CL-TRIS3.0	1817	2.51	1.45	2.91	1.09
CL-TRIS2.5	1545	2.65	1.53	3.05	1.24
CL-TRIS2.0	1274	2.67	1.54	3.07	1.37
CL-TRIS1.5	1003	2.72	1.59	3.18	1.57
CL-TRIS1.3	894	2.72	—	—	—

M_w = molecular weight, d = Bragg spacing ($2\pi/q$), a = inter columnar distance ($2d_{110}$), D = calculated pore size ($d_{100}\,(8\phi_{TRIS}/\sqrt{3}\,\pi)^{1/2}$), and ϕ_{TRIS} is the volume fraction of TRIS in the complex at the stoichio-metric ratio.

resulting in a corresponding expansion in the pore size from 0.96 to 1.57 nm. In other words, within the small stoichio-metry range, the dimension of the Col$_h$ mesophase, 'a', enlarges by 8.5%, while the pore size of the Col$_h$ mesophase, 'D', expands by 64% (Fig. 2c). By comparison, the mesophase made using rigid templates cannot accommodate stoichio-metric variations due to steric hindrance and the geometry of the interactions,[31,32] which leads us to surmise that the notable variation in our mesophase might be attributed to the

liquid nature of TRIS, which facilitates facile adjustment of volume fraction while maintaining favorable interactions with CL and preserving the overall Col$_h$ mesophase structure. In a "soft" system like CL-TRIS, associations are governed by rela-tively weak attractive interactions between CL and TRIS, such as those that drive the miscibility of polymers. Consequently, the pore size of CL-TRIS# can be finely controlled with sub-nm pre-cision by making stoichiometric changes, as long as the volume balance is maintained by stable acid–base interactions.

3.3 Fabrication of nanostructured membranes

Nanostructured membranes based on CL-TRIS#s were fabri-cated by the molecular templating approach, which involves two steps, polymerization and template removal.[11,19,21,22] The templated Col$_h$ mesophases of CL-TRIS#s were fixed by photoi-nitiated free-radical polymerization,[11,14,19] where 12 wt% of HDDMA and 1 wt% of DMPA were added as the crosslinkers and the photo-initiator. Among them, because of weak acid–base interactions and unstable structures, CL-TRIS1.5 and CL-TRIS4.0 were not able to maintain the Col$_h$ mesophase with the addition of crosslinkers, as evidenced by the dark POM images in Fig. S7.† Accordingly, polymerization was per-formed for CL-TRIS2.0, CL-TRIS2.5, CL-TRIS3.0, and CL-TRIS3.5, which could retain the Col$_h$ mesophase. After UV polymerization, rigid and transparent polymer films were

obtained (Fig. 4b and Fig. S10a†). The successful copolymerization of the co-monomer and CL was evidenced by FT-IR (Fig. 3a and Fig. S8†). Specifically, a significant reduction in IR bands at 940 cm^{-1} and 1637 cm^{-1}, corresponding to C=C–H bending and C=C stretching in the unsaturated double bonds of the citronellol moiety[19,22] respectively, is observed. In addition, an IR band corresponding to the C=C vibrations of methacrylate at 1166 cm^{-1} disappears.[33] The retention of the Col$_h$ mesophase of the polymer films was confirmed by the fan-like optical texture observed under POM (Fig. S7†) and the characteristic diffraction peak location ratio of $1 : \sqrt{3} : \sqrt{4}$ on the SAXS 1D plots (Fig. 4a, b and Fig. S10a†). Compared to the Col$_h$ mesophase, the SAXS peak positions of the polymer film

slightly shift to a lower q range, due to the expansion of the intercolumnar diameter after the addition of the co-monomer.[19,22]

The nanopores on membranes based on CL-TRIS2.0, CL-TRIS2.5, CL-TRIS3.0, and CL-TRIS3.5 were formed after selective removal of the template molecule, TRIS. 3 mg polymer films were immersed in 10 ml of 0.05 wt% NaOH aqueous solution for 73 h to selectively wash out TRIS. In the basic solution, the film surface becomes negatively charged, as demonstrated by the –O–C=O stretching vibration at 1424 cm^{-1} (Fig. 3a and Fig. S8†).[22] While the removal of TRIS cannot be directly detected by FT-IR, primarily due to the limited detectability of the FT-IR peak associated with the
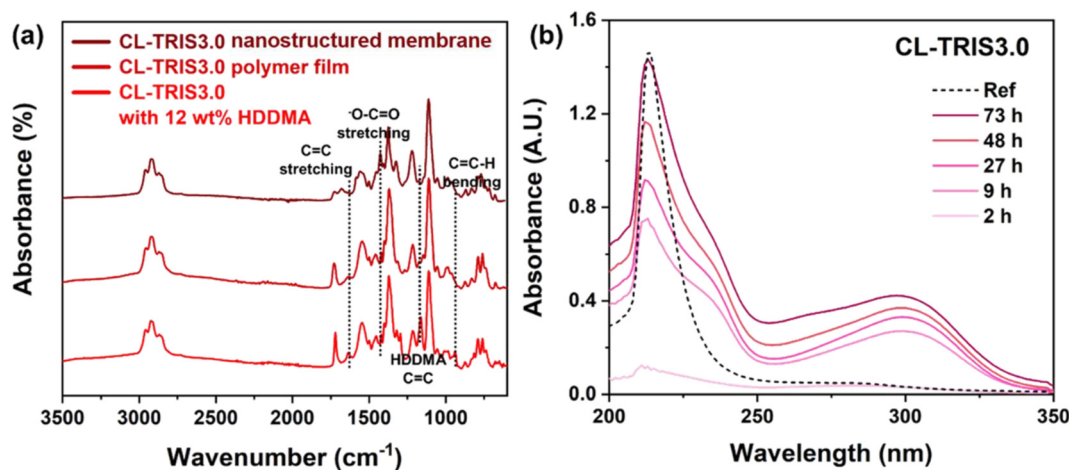

Fig. 3 (a) FT-IR spectra of the Col$_h$ mesophase with 12 wt% of HDDMA, polymer films, and nanostructured membranes based on CL-TRIS3.0. (b) UV-Vis spectrum of the dynamic release of TRIS for 73 h from the 3 mg polymer film of CL-TRIS3.0 soaked in 0.05 wt% NaOH in 10 ml of deionized water. The reference (dotted line) indicates TRIS in NaOH aqueous solution (150 μM).
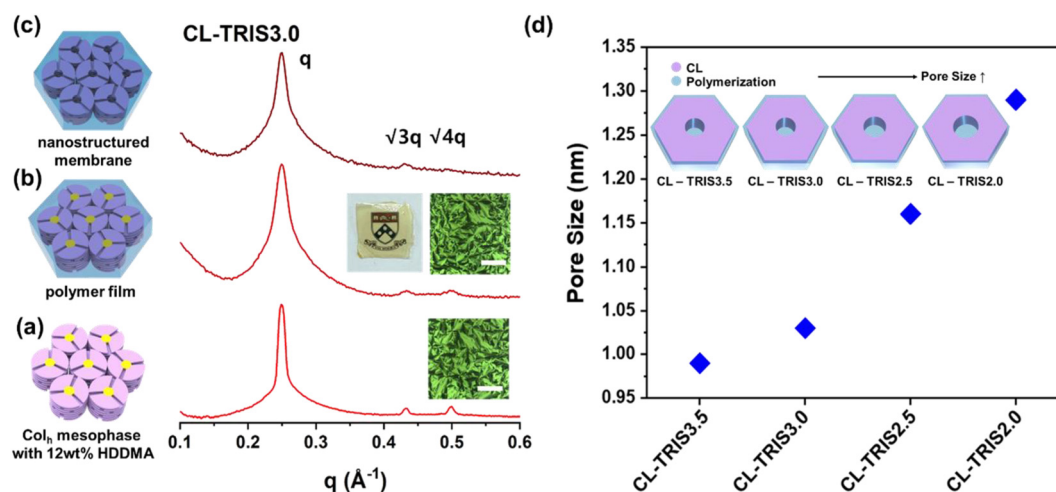

Fig. 4 SAXS 1D plots of (a) Col$_h$ mesophases with 12 wt% of HDDMA (bottom), (b) polymer films (middle), and (c) nanostructured membranes (top) for CL-TRIS3.0. The insets show the POM images of CL-TRIS3.0 before and after polymerization (the bar = 100 μm). The photo included in (b) is its respective film. (d) Pore sizes, D, correspond to the CL-TRIS3.5, CL-TRIS3.0, CL-TRIS 2.5, and CL-TRIS2.0 membranes. The inset shows a schematic diagram of the membranes with relative dimensions and pore sizes.

primary amine (–NH$_2$) interacting with the acid (–COOH),[30] the dynamic release of TRIS from the polymer films was monitored by UV-Vis spectroscopy for 73 h (Fig. 3b and Fig. S9†). The absorbance at 214 nm gradually increases and becomes stabilized after 73 h, reaching 98% of the reference line. Note that a dynamic release test extended to 96 h was also conducted, revealing an observed release rate of 98.3%. We believe that a 73 h immersion period is sufficient for subsequent adsorption experiments, as 98% of the specific surface area in the membrane samples is adequate to adsorb all dye molecules (detailed calculations are provided in the ESI†). Here, the reference line represents the absorbance of 150 μM of TRIS in 0.05 wt% NaOH solution, equivalent to the amount of TRIS contained in the 3 mg polymer films. The absorbance at around 300 nm appears to originate from the leaching of a minor quantity of unpolymerized CL or CL oligomers from the membranes into the NaOH solution.

The retention of Col$_h$ mesophases in membranes was demonstrated by SAXS 1D plots (Fig. 4c and Fig. S10b†). These membranes display the characteristic diffraction peaks representing the Col$_h$ mesophase with negligible changes in the peak position compared to the polymer films. The pore sizes of CL-TRIS3.5, CL-TRIS3.0, CL-TRIS2.5, and CL-TRIS2.0 membranes were recalculated based on the corres-

ponding SAXS result, revealing sizes of 0.99 nm, 1.03 nm, 1.16 nm, and 1.29 nm, respectively (Fig. 4d). Consequently, within this small stoichiometry range, the pore size of the nanostructured membranes can be tuned by up to 30% (Fig. 4d). Remarkably, by changing the stoichiometry in the CL-TRIS# system, the highest attainable resolution among the membranes is as fine as 0.04 nm, significantly surpassing previously reported values.[23,34] The stability of the crosslinked membranes was demonstrated by their ability to maintain film integrity after immersion in methanol for 24 h (Fig. S11†).

3.4 Dye adsorption tests

The selectivity performances of CL-TRIS2.0 and CL-TRIS3.0 nanostructured membranes were investigated by simultaneous adsorption tests using model penetrant molecules with different charges, sizes, and shapes. To effectively differentiate the performance of the CL-TRIS2.0 and CL-TRIS3.0 membranes with a pore size difference of 0.26 nm, seven dyes ranging from 0.9 nm to 2.4 nm were employed: Basacryl Red GL (BRG), Basic Orange (BO), Toluidine Blue O (TBO), Auramine Orange (AO), Crystal Violet (CV), and Tetrazolium Blue (TB) are positively charged, while Rose Bengal (RB) is negatively charged. The molecular dimensions of these dyes are summarized in Fig. 5a and Fig. S12.† The
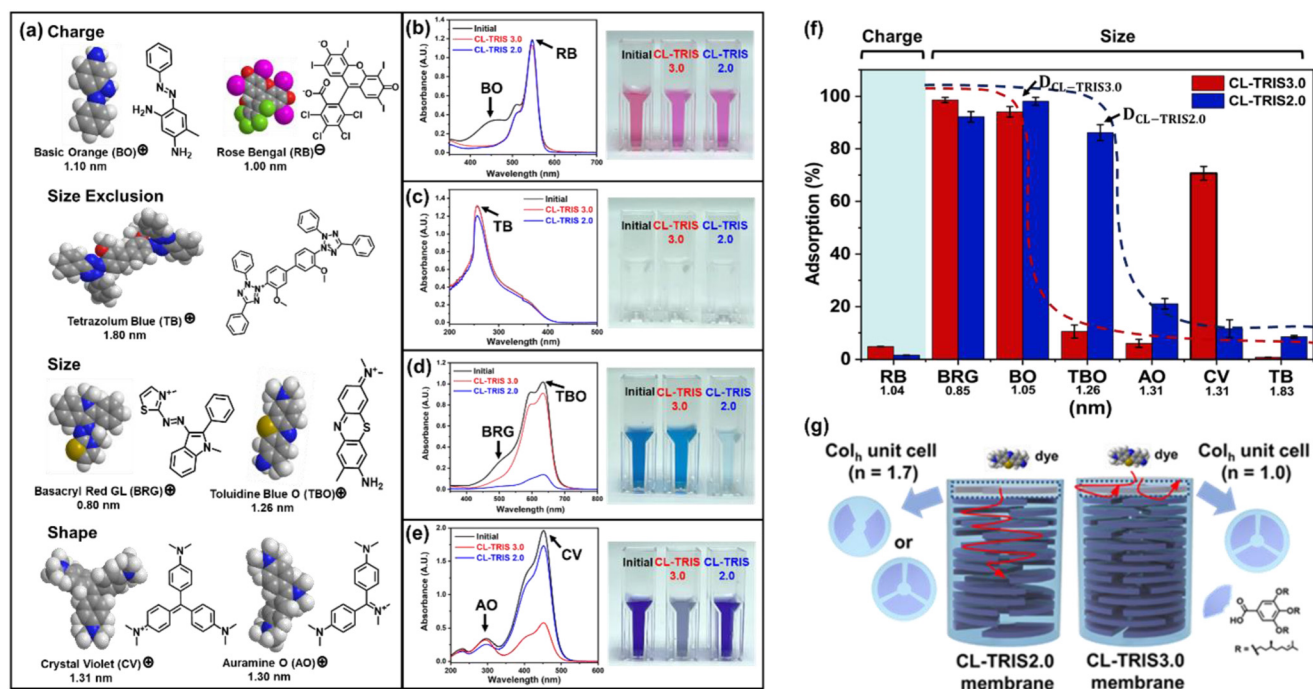

Fig. 5 (a) Molecular structures and space-filling models of dye molecules. (b) Charge-selective adsorption of BO onto nanopores of the CL-TRIS2.0 and CL-TRIS3.0 membranes from a solution of BO and RB. (c) Exclusion of TB by the nanopores of the CL-TRIS2.0 and CL-TRIS3.0 membranes. (d) Size-selective adsorption of BRG onto the nanopores of the CL-TRIS3.0 membrane while no selectivity shown by the CL-TRIS2.0 membrane from a solution of BRG and TBO. (e) Shape-selective adsorption of CV onto the nanopores of the CL-TRIS3.0 membrane while no selectivity shown by the CL-TRIS2.0 membrane from a solution of CV and AO. The inset included in the spectrum indicates a color change in the dye solutions. (f) Overall dye adsorption results of the CL-TRIS2.0 and CL-TRIS3.0 membranes based on (a)–(d), where the blue-dotted and red-dotted lines represent the dye-adsorption trends of the CL-TRIS2.0 and CL-TRIS3.0 membranes, respectively. $D_{CL-TRIS2.0}$ and $D_{CL-TRIS3.0}$ indicate the pore size of each membrane. (g) 3D-schematic diagrams indicating the Col$_h$ mesophase packing structures of the CL-TRIS3.0 and CL-TRIS2.0 membranes composed of the corresponding unit cell. n indicates the number of complexes in the Col$_h$ unit cell.

sizes indicated here represent the maximum dimensions along 3 principal axes of each dye molecule. They are determined from calculations in the Chem3D software package using the MM2 energy minimization force field. Given the geometry of pores on CL-TRIS#s membranes (*i.e.* not slit-like), the maximum dimension of the dye molecule represents the length scale that limits transport within the membranes. After simultaneous adsorption tests, the membranes retained their film integrity and remained physically stable (Fig. S13†) It is worth noting that the selectivity determined by adsorption is expected to provide an upper limit for the separation performance of the membranes, as transport under convective flow typically results in greater permeability.

The charge selectivity of the CL-TRIS2.0 and CL-TRIS3.0 membranes was established by the simultaneous adsorption of anionic RB and cationic BO (Fig. 5b). Both membranes exhibited negatively charged surfaces due to the presence of carboxylate groups resulting from the TRIS rinsing step in NaOH. After equilibrating for 2 d, both membranes demonstrated pronounced charge selectivity to cationic BO, which is evident from the substantial reduction in the 458 nm BO adsorption band, accompanied by only a slight decrease (within 5%) in the 546 nm RB adsorption band in the UV-vis spectrum. The color transition from red to pink further corroborated the strong adsorption for cationic BO due to the Gibbs–Donnan effect, despite BO having a larger dimension compared to RB.[19,35]

The size selectivity was further demonstrated by other cationic dyes. The result of size exclusion of TB (1.83 nm), larger than the pore size of both the CL-TRIS2.0 membrane (1.29 nm) and the CL-TRIS3.0 membrane (1.03 nm), is presented in Fig. 5c. The CL-TRIS3.0 membrane (red line) displayed a stable peak centered at around 258 nm after 2 d, indicative of its ability to completely reject TB. The tiny decrease in the intensity of red peak might be ascribed to slight bulk surface adsorption stemming from surface ionic interactions, while the CL-TRIS2.0 membrane (blue line) exhibited an 8.5% adsorption of TB. This higher adsorption is attributed to its larger pore relative to the CL-TRIS3.0 membrane, resulting in more exposed negatively charged active sites on the surface available for dye interaction. The color change is not noticeable because of the light-yellow color of the diluted TB solution. The size exclusion properties of the CL-TRIS2.0 membrane were further demonstrated by its complete rejection of the larger-sized dye, Alcian Blue 8G (AB8G, 2.35 nm), as shown in Fig. S14b.†

Other smaller cationic dyes were employed to further investigate the distinctions in size selectivity between the CL-TRIS2.0 membrane and the CL-TRIS3.0 membrane. Fig. 5d illustrates the simultaneous adsorption result of BRG (0.85 nm, detected at 495 nm) and TBO (1.26 nm, detected at 635 nm). The CL-TRIS3.0 membrane selectively adsorbs BRG over TBO (98% *vs.* 10%), while the CL-TRIS2.0 membrane exhibits a negligible difference in the adsorption of BRG and TBO (92% *vs.* 86%). This observation suggests that the smaller-sized BRG can diffuse more rapidly than the larger-sized TBO

and pre-occupies most of the active sites on CL-TRIS3.0 membrane, whereas the relatively larger pore size of the CL-TRIS2.0 membrane impedes clear size selectivity between RBG and TBO. The slight adsorption of TBO on the CL-TRIS3.0 membrane is likely due to adsorption on the exposed bulk surface of the sample. It is also possible that TBO could diffuse into grain boundaries, the relatively disordered regions between ordered grains. In a separate simultaneous uptake experiment involving a mixture of TBO and larger-sized Rhodamine 6G (RH6G, 1.63 nm), the CL-TRIS2.0 membrane exhibits clear size selectivity for TBO compared to RH6G (86.2% *vs.* 9.5%) (Fig. S14d†).

All results of the dye adsorption experiments are summarized in Fig. 5f. The blue- and red-dotted lines represent the trends in dye adsorption of the CL-TRIS2.0 membrane and the CL-TRIS3.0 membrane, respectively. Remarkably, both membranes exhibited the capacity to discern sub-nm size differences among the penetrants. Furthermore, the 0.26 nm difference in pore size between the membranes yields a clear distinction in size selectivity for specific sizes of the dye. Based on the adsorption outcomes, the size cut-off of the CL-TRIS2.0 membrane and the CL-TRIS3.0 membrane was estimated to be around 1.26 nm and 1.05 nm, based on the adsorption results, closely aligning with previous calculations. The difference in the size cut-off can be attributed to the different packing structures internal of the constituent Col_h unit cell. Specifically, the structures in the Col_h unit cell can be described by a parameter 'n', which is the number of complexes in the hypothetical Col_h unit cell.[30,36] Details regarding the calculation of n are included in the ESI.† The n-value of CL-TRIS3.0 was calculated to be 1, suggesting a disc-shaped Col_h unit cell with a geometry where all three amine groups of TRIS coordinate with CLs (C3 geometry) (Fig. 5g). On the other hand, the n-value of CL-TRIS2.0 was calculated to be 1.7, indicating that its columnar structure might comprise a blend of saturated C3 geometric unit cells and unsaturated geometric unit cells, where only two amine groups of TRIS coordinate with CLs and 2 complexes are distributed within a hypothetical Col_h unit cell (C2 geometry). As a result, CL-TRIS3.0 has more chances to form disconnected small channels due to the densely packed columnar structure based on C3 geometric unit cells, resulting in higher rejection for smaller penetrants. Conversely, the structure of CL-TRIS2.0 appears to be less dense, formed through a combination of C2, and C3 geometric unit cells, allowing for the penetration of penetrants through continuously connected large channels.

Furthermore, it is worth noting that the adsorption results for CV do not align with the red-absorbance trend line of the CL-TRIS3.0 membrane (Fig. 5f). Despite CV (1.31 nm) and AO (1.30 nm) having similar sizes, the CL-TRIS3.0 membrane exhibited a significantly stronger adsorption of CV (band at 453 nm) over AO (band at 297 nm) (71% *vs.* 6%) (Fig. 5e). Conversely, the CL-TRIS2.0 membrane rejects mostly CV and AO without showing a clear selectivity (12% *vs.* 21%), consistent with the expected blue trend line. Based on these observations, we surmise that the CL-TRIS3.0 membrane may

possess shape selectivity to 'propeller-shaped' penetrants. This supposition is supported by the unique propeller-shape of CV, distinct from other dyes used in the previous experiments. To validate this hypothesis, further simultaneous uptake experiments were conducted using mixtures of banana-shaped AO and propeller-shaped dyes of similar size to AO (Fig. S15†). Specifically, Victoria Pure Blue BO (VPB, 1.44 nm) and Brilliant Green (BG, 1.43 nm) were employed as model propeller-shaped dyes mixed with AO. Consistent with the results of the CV–AO mixture, the CL-TRIS3.0 membrane exhibits stronger adsorption to the larger, but propeller-shaped VPB and BG, compared to the slightly smaller-sized AO. In contrast, the adsorption performance of the CL-TRIS2.0 membrane is primarily influenced by size, showing similar adsorption abilities to AO, CV, VPB, and BG. The shape selectivity of the CL-TRIS3.0 membrane may be related to physical differences that arise in the pore due to the stoichiometry with which the relatively rigid ligand is bound by the flexible core (Fig. 5g). We surmise that the binding of the three propyl amine groups on each molecule of TRIS by stoichiometric equivalents of the ligand predisposed the system to adopt C3 geometry, particularly given the tendency of the aromatic groups of the ligand to form planar stacks. Removal of TRIS after immobilization of the ligand by crosslinking would leave a core that is C3 geometric or propeller-shaped in its cross-section. It is conceivable that such a propeller-shaped channel in CL-TRIS3.0 contributes to its preference for the adsorption of propeller-shaped dyes over other shaped dyes. In contrast, we do not anticipate the CL-TRIS2.0 membrane to exhibit C3 geometry, so it does not preferentially adsorb propeller-shaped dyes. Instead, its adsorption behavior is dominated simply by size selectivity. In general, delineating the effects of shape *versus* chemical specificity driven by preferential interaction is difficult. It is possible that the larger uptake of CV in the CL-TRIS3.0 membrane could be associated with the preferential interaction of aromatic groups in the dye and along the pore wall. However, the prevalence of aromaticity in AO and exposed aromatic groups on the pore wall of the CL-TRIS2.0 membrane suggests otherwise. It may be sufficient to conclude that the commensurability of the propeller-shaped pore offered by CL-TRIS3.0 enables favorable molecular interactions that facilitate greater adsorption. It is worth noting again that the CL-TRIS3.0 membrane adsorbs a significantly larger amount of dye molecules (CV) that is larger than the control (AO) and the CL-TRIS2.0 membrane, despite having similar pore wall chemistry and a larger pore, adsorbs a much smaller amount of the smaller dye (CV) and more of the larger, more linear species (AO). In future investigations, we aim to delve deeper into the mechanisms underlying local structural and morphological variations in the stoichiometry of this Col_h mesophase through molecular dynamics simulations and provide a more comprehensive understanding of our membranes' shape selectivity properties.

The adsorption capacity of nanostructured membranes towards dye molecules is related to their specific surface area, S_v, and functional group density, σ. These parameters are determined based on membranes' structural parameters, including effective pore diameter, relative density between the template and ligands, and mass fractions of the template and ligands (detailed calculation is provided in the ESI†). For the CL-TRIS3.0 membrane, the S_v was estimated to be 450 m² g⁻¹ and the σ was estimated to be 2.79 nm⁻². For the CL-TRIS2.0 membrane, the S_v was estimated to be 534 m² g⁻¹ and the σ was estimated to be 2.28 nm⁻². Based on the S_v value, the available area of 3 mg of Cl-TRIS3.0 is 1.35 m² and that of CL-TRIS2.0 is 1.60 m², without consideration of the external film surface area (4.5×10^{-4} m²). Taking the largest-sized dye TB as an example, we assume the maximum projected molecular area for TB of 2.96 nm² and a maximum packing fraction of 0.55 with random adsorption.[37] Thus, achieving complete adsorption of 3.5×10^{-7} moles TB in a 7 mL test solution requires approximately 1.13 m², which is smaller than the estimated available internal surface area of each test film but much larger than the external film surface area. Complete uptake of TB would lead to an areal density of 0.2 nm⁻², far less than the areal density of functional groups on the CL-TRIS nanostructured membrane, σ, estimated before. Even though there are uncertainties in the estimation, the results are consistent with the notion that the rejection of larger-sized dye molecules by the CL-TRIS nanostructured membranes is due to the selectivity of the membrane pores, and not due to a lack of the internal surface against which the molecules would adsorb. It also underscores that the adsorption predominantly occurs within the internal channels rather than solely on the external surface.

4. Conclusions

In summary, we developed a pore size-tunable nanostructured membrane based on the plant-derived citronellol compound. The tunability was achieved by changing the stoichiometry between the complementary pair of CL and TRIS in the self-assembled Col_h mesophase (CL-TRIS#, where # is a stoichiometric ratio of CL to TRIS). By varying the stoichiometry from 4.0 to 1.5, different dimensions of the Col_h mesophase could be attained. Specifically, the intercolumnar distance of the Col_h mesophase increased by 8.5%, while the pore size expanded by 64%, which might be attributed to the flexible liquid aspect of TRIS. Subsequently, nanostructured membranes based on CL-TRIS3.5, CL-TRIS3.0, CL-TRIS2.5, CL-TRIS2.0 were fabricated by a molecular templating approach. We found that the tunable pore size of these Col_h mesophase membranes ranged from 1.0 to 1.3 nm with sub-nm resolution, which is much smaller than the previously reported values. CL-TRIS3.0 and CL-TRIS2.0 membranes exhibited distinct size selectivity despite a narrow pore size gap of only 0.26 nm, as confirmed by simultaneous dye uptake experiments. In particular, the CL-TRIS3.0 membrane demonstrated the potential for shape selectivity to propeller-shaped penetrants. Therefore, the pore geometry of Col_h membranes can be precisely controlled depending on the stoichiometry,

offering promising prospects for advancements in the realm of nanostructured membranes in analytical chemistry or nanofiltration. The high selectivity of our nanoporous membranes suggests their potential for selective adsorption of specific solutes among the molecules of similar sizes or shapes at the nanometer scale, with possible applications in water purification. This approach demonstrates several sustainability-related aspects, underscored by the use of plant-derived ligands and the ease of template removal without the need for organic solvents.

In the future, we would like to further explain the mechanism of local structural and morphological variations in the stoichiometry in this self-assembled Col_h mesophase by molecular dynamics simulations. We believe that these simulations will provide quantitative and theoretical insights into the self-assembly mechanisms, which could not only enhance our understanding of the Col_h system, but also contribute to advancements in other liquid crystal self-assembly systems.

Author contributions

Ruiqi Dong and Na Kyung Kim: conceptualization, data curation, formal analysis, investigation, visualization, writing – original draft, and review and editing. Zhuan Yi: synthesis investigation and writing – review and editing. Chinedum O. Osuji: conceptualization, formal analysis, and writing – review and editing.

Data availability

The data supporting this article have been included as part of the article or its ESI.†

Conflicts of interest

There are no conflicts of interest to declare.

Acknowledgements

References

1 X. Lu, X. Feng, J. R. Werber, C. Chu, I. Zucker, J.-H. Kim, C. O. Osuji and M. Elimelech, *Proc. Natl. Acad. Sci. U. S. A.*, 2017, **114**, E9793–E9801.

2 A. S. Arico, P. Bruce, B. Scrosati, J.-M. Tarascon and W. Van Schalkwijk, *Nat. Mater.*, 2005, **4**, 366–377.

3 X. Huang, T. Shen, T. Zhang, H. Qiu, X. Gu, Z. Ali and Y. Hou, *Adv. Energy Mater.*, 2020, **10**, 1900375.

4 J. Hu, T. W. Odom and C. M. Lieber, *Acc. Chem. Res.*, 1999, **32**, 435–445.

5 D. Park, C. O. Osuji and J. W. Kim, *Small Methods*, 2023, **7**, 2201195.

6 D. Park, J. W. Kim, K. Shin and J. W. Kim, *Carbohydr. Polym.*, 2021, **272**, 118459.

7 Y. Shen, *Global Chall.*, 2018, **2**, 1800043.

8 D. Pochan and O. Scherman, *Journal*, 2021, **121**, 13699–13700.

9 D. Lombardo, P. Calandra, L. Pasqua and S. Magazù, *Materials*, 2020, **13**, 1048.

10 C. J. Edwards-Gayle and I. W. Hamley, *Org. Biomol. Chem.*, 2017, **15**, 5867–5876.

11 O. Q. Imran, N. K. Kim, L. N. Bodkin, G. E. Dwulet, X. Feng, K. Kawabata, M. Elimelech, D. L. Gin and C. O. Osuji, *Adv. Mater. Interfaces*, 2021, **8**, 2001977.

12 M. Foston, C. Hubbell, D. Y. Park, F. Cook, Y. Tezuka and H. W. Beckham, *Angew. Chem., Int. Ed.*, 2012, **51**, 1849–1852.

13 O. Q. Imran, P. Li, N. K. Kim, D. L. Gin and C. O. Osuji, *Chem. Commun.*, 2021, **57**, 10931–10934.

14 Y. Zhang, R. Dong, U. R. Gabinet, R. Poling-Skutvik, N. K. Kim, C. Lee, O. Q. Imran, X. Feng and C. O. Osuji, *ACS Nano*, 2021, **15**, 8192–8203.

15 X. Feng, Q. Imran, Y. Zhang, L. Sixdenier, X. Lu, G. Kaufman, U. Gabinet, K. Kawabata, M. Elimelech and C. O. Osuji, *Sci. Adv.*, 2019, **5**, eaav9308.

16 C. Lee, D. Ndaya, R. Bosire, N. K. Kim, R. M. Kasi and C. O. Osuji, *J. Am. Chem. Soc.*, 2021, **144**, 390–399.

17 P. Li, M. I. Reinhardt, S. S. Dyer, K. E. Moore, O. Q. Imran and D. L. Gin, *Soft Matter*, 2021, **17**, 9259–9263.

18 P. W. Majewski, M. Gopinadhan and C. O. Osuji, *Soft Matter*, 2013, **9**, 7106–7116.

19 X. Feng, K. Kawabata, G. Kaufman, M. Elimelech and C. O. Osuji, *ACS Nano*, 2017, **11**, 3911–3921.

20 J. Kloos, N. Joosten, A. Schenning and K. Nijmeijer, *J. Membr. Sci.*, 2021, **620**, 118849.

21 I. Gracia, P. Romero, J. L. Serrano, J. Barberá and A. Omenat, *J. Mater. Chem. C*, 2017, **5**, 2033–2042.

22 G. M. Bögels, J. A. Lugger, O. J. Goor and R. P. Sijbesma, *Adv. Funct. Mater.*, 2016, **26**, 8023–8030.

23 S. Bhattacharjee, J. A. Lugger and R. P. Sijbesma, *Macromolecules*, 2017, **50**, 2777–2783.

24 J. A. Lugger, P. P. Marín San Román, C. C. Kroonen and R. P. Sijbesma, *ACS Appl. Mater. Interfaces*, 2021, **13**, 4385–4392.

25 M. A. Shannon, P. W. Bohn, M. Elimelech, J. G. Georgiadis, B. J. Mariñas and A. M. Mayes, *Nature*, 2008, **452**, 301–310.

26 J. Lugger, D. J. Mulder, R. Sijbesma and A. Schenning, *Materials*, 2018, **11**, 104.

27 J. Sun, C. Lee, C. O. Osuji and P. Gopalan, *Macromolecules*, 2021, **54**, 9542–9550.

28 K. Toth, S. Bae, C. O. Osuji, K. G. Yager and G. S. Doerk, *Macromolecules*, 2021, **54**, 7970–7986.

29 C. Lee, D. Ndaya, R. Bosire, U. R. Gabinet, J. Sun, P. Gopalan, R. M. Kasi and C. O. Osuji, *Macromolecules*, 2021, **54**, 3223–3231.

30 T. Noguchi, K. Kishikawa and S. Kohmoto, *Bull. Chem. Soc. Jpn.*, 2008, **81**, 778–783.

31 A. Kohlmeier and D. Janietz, *Chem. Mater.*, 2006, **18**, 59–68.

32 A. Kohlmeier and D. Janietz, *Chem. – Eur. J.*, 2010, **16**, 10453–10461.

33 Y. Kang, K. Cheong, K.-A. Noh, C. Lee and D.-Y. Seung, *J. Power Sources*, 2003, **119**, 432–437.

34 S. Bhattacharjee, J. A. M. Lugger and R. P. Sijbesma, *Chem. Commun.*, 2018, **54**, 9521–9524.

35 J. Waniewski, M. Pietribiasi and L. Pstras, *Sci. Rep.*, 2021, **11**, 22150.

36 L. Vogel, D. Janietz, M. Prehm and C. Tschierske, *Soft Matter*, 2017, **13**, 7188–7196.

37 S. Ardizzone, G. Gabrielli and P. Lazzari, *Colloids Surf., A*, 1993, **76**, 149–157.